Evaluation of a field cancerization model using parenchymal analysis

B.Sc. Angie Nicole Hernández Durán

A Thesis Presented in Fulfillment of the Requirements for the Degree of Master of Physics

Advisors:

Ph.D. Said David Pertuz Arroyo

Ph.D. David Alejandro Miranda Mercado

Universidad Industrial de Santander

Escuela de Física

Facultad de Ciencias

2023

Dedication

To my husband, for arriving in a victory rose to hang around in the tunnels.

To my sister, for giving me hope.

To my parents, for giving me everything.

Acknowledgments

I express my deepest gratitude to professors Said and David for their invaluable guidance.

Contents

List of Figures

List of Tables

Resumen

Título: Evaluación de un modelo de campo carcinogénico usando análisis parenquimatoso [*]

Autores: Angie Nicole Hernández Durán [**]

Palabras Clave: Evaluación de riesgo de cáncer de mama, análisis parenquimatoso, mamografía, efecto de campo carcinogénico

Descripción: El análisis parenquimatoso ha mostrado un desempeño notable para la evaluación del riesgo de cáncer de mama, estableciéndose como una herramienta prometedora para esta tarea. Sin embargo, su principio de funcionamiento no es conocido aún. El *efecto de campo carcinogénico* es un fenómeno asociado con cambios genéticos y epigenéticos en grandes volúmenes de células, que las ponen en el camino de malignidad incluso antes de la aparición de signos reconocibles de cáncer. Este fenómeno se ha estudiado durante casi 70 años y la evidencia sugiere que puede inducir cambios en las propiedades bioquímicas y ópticas del tejido. En este trabajo exploramos la idea de que la cancerización del campo es el principio de trabajo subyacente del análisis parenquimatoso. Nuestra hipótesis es que los cambios genéticos y epigenéticos extendidos debido al campo carcinogénico tienen un impacto en la bioquímica de los tejidos mamarios, que luego se reflejan en los patrones parenquimatosos de las imágenes mamográficas. Para testear esta hipótesis, nuestro objetivo es comprobar si el efecto de cancerización de campo tiene repercusiones detectables a nivel mamográfico, mediante el análisis de las características parenquimatosas de la mama. Para probar esta idea, diseñamos un experimento *in silico*: Basándonos en la literatura sobre el efecto de campo carcinogénico, inicialmente propusimos un modelo que modifica las propiedades ópticas del tejido de una cohorte de 60 phantoms mamarios virtuales en 3D. Simulamos imágenes mamográficas de phantoms con y sin efecto de campo carcinogénico y evaluamos sus diferencias mediante análisis parenquimatoso. Específicamente, extrajimos 33 características de tex-

---

[*] Trabajo de grado

[**] Facultad de Ciencias, Escuela de Física.

tura del área de la mama y analizamos sus diferencias estadísticas y equivalencia estadística utilizando la prueba t, la prueba de rangos con signos de Wilcoxon y la prueba de Kolmogorov-Smirnov. También realizamos una prueba de discriminación mediante análisis de regresión logística multinomial con regularización de Lasso. Esta investigación tiene como objetivo identificar los límites en los que se pueden detectar posibles alteraciones en el tejido mamario debido al efecto de campo carcinogénico a través del análisis parenquimatoso. Nuestros resultados pueden proporcionar evidencia para apoyar o rechazar la idea de que el efecto de campo carcinogénico es un principio de trabajo subyacente factible detrás del desempeño distintivo del análisis parenquimatoso en la evaluación de riesgo de cáncer de mama.

Abstract

Title: Evaluation of a field cancerization model using parenchymal analysis [*]

Author: Angie Nicole Hernández Durán [**]

Keywords: Breast cancer risk assessment, parenchymal analysis, mammography, field cancerization

Description: Parenchymal texture analysis has shown a remarkable performance for breast cancer risk assessment, establishing itself as a promising tool for this task. However, the working principles behind it are not well understood yet. *Field cancerization* is a phenomenon associated with genetic and epigenetic changes in vast volumes of cells, which put them on path of malignancy even before the apparition of recognizable cancer signs. This phenomenon has been studied for nearly 70 years and evidence suggests that it can induce changes in the biochemical and optical properties of the tissue. In this work we explore the idea that field cancerization is the underlying working principle of parenchymal texture analysis. We hypothesize that the extended genetic and epigenetic changes due to field cancerization have an impact in the biochemistry of the breast tissues, which are then reflected in the parenchymal patterns of mammography images. To test this hypothesis, our objective is to test whether the field cancerization effect has repercussions that are detectable at the mammography level, via the analysis of the parenchymal features of the breast. To test this idea we designed an *in silico* experiment. Experiment: Based on the literature on field cancerization, we first proposed a model that modifies the optical properties of the tissue of a cohort of 60 virtual 3D breast phantoms. We simulated mammography images from phantoms with and without field cancerization, and assessed their differences using parenchymal analysis. Specifically, we extracted 33 parenchymal features from the breast area and analyzed their statistical differences and statistical equivalence using t-test, Wilcoxon signed rank test

---

[*] Master's Thesis

[**] Facultad de Ciencias, Escuela de Física

and Kolmogorov-Smirnov test. We also performed a discrimination test using multinomial logistic regression analysis with Lasso regularization. This investigation aims to identify the limits at which potential alterations in the breast tissue due to field cancerization can be detected via parenchymal analysis. Our results can provide evidence to support or reject the idea that field cancerization is a feasible underlying working principle behind the distinctive performance of parenchymal texture analysis in breast cancer risk assessment.

Introduction

Breast cancer is among the most prolific cancers in women worldwide and it is one of the leading causes of cancer deaths in women Siegel et al. (2022). Routine screening mammography on the high risk population (usually women above 40 years old) is the most common practice for early detection of this disease, which is crucial to decrease mortality and improve patient prognosis Coleman (2017). A helpful practice for early detection is *risk assessment*. Clinically recognized biomarkers, such as the genes BRCA 1/2 and clinical history, have been used both standalone and in combination to build risk assessment models such as the Gail model Wang et al. (2018). Still, the predictive power of risk models remains limited in the general population Amir et al. (2003). Alternatively, the use of biomarkers extracted from mammography images has proven valuable for breast cancer risk assessment; one of the main branches of this practice is known as *parenchymal texture analysis*.

In parenchymal texture analysis, computerized texture features extracted from mammograms are used to construct predictive models via machine learning techniques Gastounioti et al. (2016). Diverse studies have showcased the potential of parenchymal analysis for breast cancer risk assessment Li et al. (2007); Kontos et al. (2019); Li et al. (2019a). The texture features used in parenchymal analysis are extracted from regions of interest (ROIs) all over the breast area in the mammogram. This characteristic suggests that the relevant textural information for risk assessment can be found in a vast area, despite cancer lesions usually appearing in localized foci.

The underlying working mechanism of parenchymal texture analysis for breast cancer risk assessment is still not understood. One hypothesis, however, points to the *Field Cancerization effect* as the possible explanation Miranda and Pertuz (2020). Field cancerization was initially proposed in 1953 by Slaughter et al. Slaughter et al. (1953). While studying epidermoid carcinoma of the oral cavity, Slaughter found that the seemingly healthy tissue surrounding malignant tumors presented abnormalities, and he named this phenomenon *field cancerization*. Since then, the term has been used for similar phenomena in cancers of different parts of the body. Pertaining the breast, field cancerization can be defined as the molecular alterations present on a relatively extensive region of otherwise histologically normal tissue, related to the eventual development of cancer Heaphy et al. (2009). Molecular evidence of field cancerization has been gathered for different organs Heaphy et al. (2009); Wistuba et al. (1999); Ushijima (2007); Nonn et al. (2009), and it has been studied on different imaging modalities Campbell et al. (1995); Subramanian et al. (2009); Damania et al. (2012); Bugter et al. (2019), showing that it produces alterations in some of the optical parameters of the organ tissues.

In this work we hypothesize that the extended biochemical alterations of the breast tissue due to field cancerization effect are identifiable via computerized analysis of the visual parenchymal patterns in radiological images, which are detectable through parenchymal texture analysis Miranda and Pertuz (2020).

To test our hypothesis we performed an *in silico* experiment that used virtual breast phantoms and digital mammography simulation. We conducted our study in three phases: 1. Literature review: we reviewed the available literature on field cancerization as a general concept and field cancerization in mammary tissue, and proposed a mathematical model for field cancerization. 2. Simulation: we generated a cohort of voxelized virtual breast phantoms with and without our field cancerization model; from these, we obtained digital mammography images by simulating X-ray propagation in biological tissue. 3. Analysis: we extracted computerized, parenchymal texture features from the breast area of each mammogram, and used t-test, Wilcoxon signed rank text and Kolmogorov-Smirnov test to assess for statistically significant differences, and an equivalence test to assess likeness; we additionally tested the discriminability of the parenchymal texture features using multinomial regression analysis. Our aim was to evaluate the effect that our proposed field cancerization model has on the radiological patterns of mammographic images. The codes are available in *https://github.com/AngieNicole-Hernandez/Breast-Phantom-Analysis-Tools*

Our experiments provide evidence on the feasibility of detecting systematical differences due to field cancerization through the analysis of parenchymal features. These results could provide support to our hypothesis, which would further the understanding of the role of parenchymal analysis for breast cancer risk assessment. Such a scenario would link radiological texture features with molecular biomarkers that have been studied for breast cancer risk assessment.

This research was part of the project “Software de análisis parenquimatoso de imágenes mamográficas para la estimación de riesgo de cáncer de seno” (Minciencias, code 110284467139).

1. Objectives

General objective

- To evaluate the effect of the changes of the physical parameters of the tissue, due to the field cancerization effect, on the radiological patterns of mammographic images of the breast.

Specific objectives

- To propose of a mathematical model to represent the effect of field cancerization in mammographic images.

- To identify a suitable virtual breast simulator for the implementation of the aforementioned model.

- To produce a virtual cohort o patients that reflect the characteristics of a set of real population.

- To perform breast cancer risk assessment using parenchymal analysis and evaluate the effect of the mathematical model proposed.

2. Theoretical background

In this section, we review the relevant concepts in which we base our hypothesis and the proposal of our model: mammographic image analysis and the evidence of field cancerization.

2.1. Mammographic Image Analysis

Breast cancer risk assessment is the practice of assigning a risk score of developing breast cancer in the upcoming years to a woman. Before the appearance of visible signs, it is not trivial to visually assess a woman's risk of developing cancer. Biomarkers such as woman's history and genetic characteristics have been used for the construction of risk models, but their predictive power in the general population leaves substantial room for improvement Amir et al. (2003). In 1976, Wolfe attempted the classification of mammograms according to the distribution of internal tissue and theorized that these categories would be associated with breast cancer risk Wolfe (1976). Wolfe's concept of categorizing mammograms according to their appearance gave way to numerous studies on breast cancer risk assessment based on mammography Hernández et al. (2021). The initial categorization practice, which suffered from human fatigue and human interpretation subjectivity, has evolved into the modern breast cancer risk assessment via computerized image analysis Hernández et al. (2021). This area is currently divided in two big branches: breast density estimation and parenchymal analysis.

Research on breast density estimation is motivated by the substantial evidence linking breast composition with breast cancer risk McCormack and dos Santos Silva (2006); Boyd et al. (2007, 2010). These methods focus on the evaluation of the percentage of dense tissue inside the breast from a mammogram, either at the area or volume level. Area based methods use pixel classification through different means to discriminate between dense and non-dense tissue. The bulk of these methods can be classified into thresholding, clustering and statistical model building methods He et al. (2015). More recently, deep learning models have also been built for the estimation of breast percent density Lee and Nishikawa (2018); Ahn et al. (2017), with encouraging performance. Volume based methods usually take on physical image formation models for their estimations, and require further information about the acquisition parameters that area methods can overlook van Engeland et al. (2006); Hartman et al. (2008); Highnam et al. (2010). Within the density estimation methods, we can also include methods that categorize mammograms according to different criteria, which are still based on breast density. These usually account for breast percent density and mammographic appearance, and use these features to perform the categorization Tzikopoulos et al. (2011); Ben-Ari et al. (2016); He et al. (2016); Antonelli et al. (2019); Lehman et al. (2019); Li et al. (2019b); Gandomkar et al. (2019)

On the side of parenchymal analysis, these techniques take advantage of the information encoded in mammographic images. Here, quantitative texture features are extracted from a region of interest (ROI) withing the breast area of the mammogram, and they are used to build risk models via machine learning techniques Byng et al. (1997); Huo et al. (2000). These methods can be categorized into feature-based and deep learning-based. Deep learning-based techniques have shown promising results Li et al. (2017). On this work, however, we do not consider these methods since the texture features in them are implicit, not allowing for the assessment of the effect of field cancerization on specific radiomic features. Feature-based methods, on the other hand, explicitly

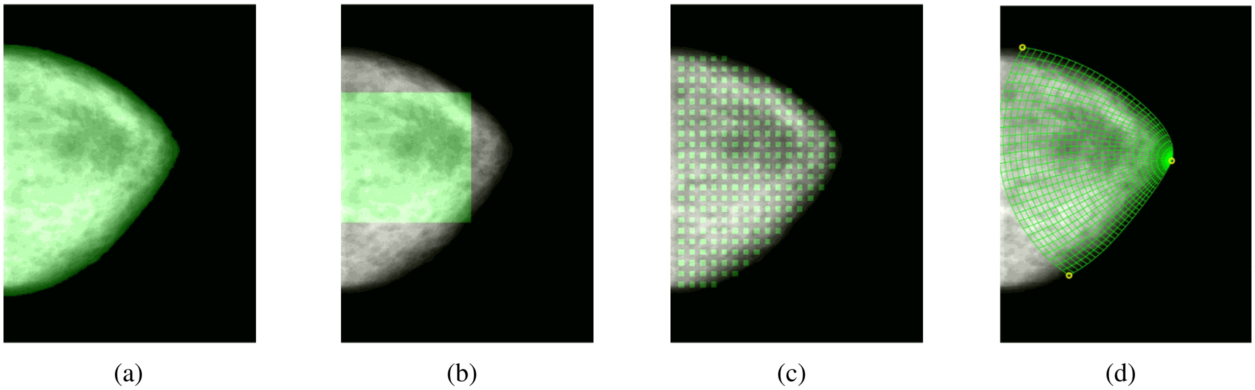
(a) (b) (c) (d)

Figure 1. Most common ROIs used for parenchymal analysis. a) Whole breast. b) Largest circumscribed square. c) Lattice-based. d) Polar-based.

take specific texture features as input, allowing the further analysis of such, and which have also shown distinctive performance Li et al. (2014); Zheng et al. (2015); Pertuz et al. (2019b); Nebbia et al. (2019).

There have been discussions on whether ROI selection has an impact on the performance of parenchymal analysis Li et al. (2004); Gastounioti et al. (2018); Africano et al. (2020). The main regions used are whole breast, largest circumscribed square, lattice-based sampling and polar-based selection (figure 1). While the use of each is supported by different arguments, all these ROIs show that parenchymal analysis is usually performed over extended areas of the breast. This was recently backed by the findings of Liu et al. Liu et al. (2020). In this research, the authors studied the effect that training data could have in a deep learning algorithm for breast cancer risk assessment. The authors found that, when the network was trained using images that contained early cancer signs, the model extracted relevant features from a relatively small area around these signs. On the other hand, when the network was trained with a dataset that did not contain any early cancer signs, the area from where relevant features were extracted was significantly more extensive than in the previous case. The latter model also showed a better performance for long-term risk assessment estimation (mammograms from one up to five years before diagnosis). These findings indicate how the cues of interest for breast cancer risk assessment span over tissues beyond the limits where the cancerous mass eventually develops, which is in line with the current understanding of field cancerization (see next section). Once the desired ROI has been selected, a predetermined set of texture features are extracted from it. These features can be categorized into statistical features Amadasun and King (1989), Gray-level co-occurrences Haralick et al. (1973), Gray-level run lengths Chu et al. (1990) and and Spectral features Li et al. (2007).

2.2. Field cancerization

Cancer is an umbrella term to refer to a large number of diseases in which abnormal cells multiply uncontrollably, usually creating tumors and interfering with the normal functionality of organs. In some cases, the abnormal cells have the ability to propagate to locations and organs beyond their onset Gabriel (2007). The origins of cancer imply genetic and epigenetic changes. When cancer is overt, these modifications are present in the surrounding tissue, however it is believed that these early epigenetic changes can also be observed in subjects at risk of developing cancer Shen et al. (2005); Yan et al. (2006); Curtius et al. (2018). The observation of these aberrations in histologically normal tissue has been labeled *field cancerization*.

This concept was first proposed in 1953 by Slaughter, stating from his observations on oral epidermoid carcinoma that ⟨⟨it would appear that epidermoid carcinoma of the oral stratified squamous epithelium originates by process of “field cancerization”, in which an area of the epithelium has been preconditioned by an as-yet-unknown carcinogenic agent⟩⟩ Slaughter et al. (1953). Since then, the concept has evolved and adapted to cancer on different organs and has been supported by numerous works. In the case of breast cancer, ⟨⟨field cancerization presently denotes the occurrence of molecular alterations in histologically normal tissues surrounding areas of overt cancer⟩⟩ Heaphy et al. (2009).

Heaphy et al. Heaphy et al. (2009) gathered the molecular evidence of field cancerization in breast cancer up until 2009. These include genetic aberrations such as allelic imbalance and loss of heterozygosity; epigenetic changes in processes such as promoter methylation and histone acetylation; and expressional aberrations in aspects such as G-coupled chemokine receptors and signal transductors. It is worth mentioning that these molecular markers, measured in histologically normal tissue, are also present in cancerous tissue. The authors reaffirm that these aberrations, while subtle for the time being, may set the cells on a pathway to malignancy and could serve as markers of disease risk. Different ideas regarding the practical use of this information on breast cancer have surfaced, such as consideration of this effect in surrounding tissue before proceeding with cancer removal surgery to avoid cancer re-incidence Rivenbark and Coleman (2012); Dworkin et al. (2009).

Field cancerization has not been widely studied in imaging modalities. However, one of the first mentions of field cancerization detection using an imaging modality was made in 1995 by Campbell et al. Campbell et al. (1995); the authors studied the tumor stage of squamous cell carcinoma of the oral cavity using magnetic resonance imaging. Based on the field cancerization theory, the authors stated that the imaging system used could detect areas of dysplasia away from the cancerous margins.

More recently, different spectroscopy modalities have been used to study field cancerization. In 2009, Subramanian et al. Subramanian et al. (2009) used partial wave microscopic spectroscopy to study cells from pancreatic cancer patients, finding that cells from patients had a higher disorder strength coefficient (L_d), a parameter related to average refractive index of the cells (n_0), than cells from control samples. In 2012, Damania et al. Damania et al. (2012) came to the same conclusion using partial wave spectroscopy in patients with precancerous lesions of the colon. These findings suggest that L_d could be a marker for field cancerization of pancreas and colon cancer. Bugter et al. Bugter et al. (2019), focusing on the optical detection of field cancerization of patients with lung cancer, studied the buccal mucosa using Multidiameter single-fiber reflectance spectroscopy. This imaging system allows the user to obtain two scattering parameters: the reduced scattering coefficient μ_s' and the phase function parameter γ; these are closely related to the nano-architecture of the tissue. The authors found that the μ_s of the buccal mucosa of cancer patients was higher than in control subjects.

In 2016, Spicer et al. Spicer et al. (2016) studied tumor progression in the context of tissue microenvironment, specifically how the changes in the micro and nano-scale structure of the extracellular matrix affect colon cancer cell growth, using inverse spectroscopic optical coherence tomography. They measured the mass density correlation shape factor D of colon cancer cells in different substrates; the parameter D is related to the backscattering coefficient μ_b via the wavenumber k ($\mu_b \propto k^{4-D}$). The results showed an increase in D when the cells were in a highly cross-linked substratum.

While the evidence just presented was gathered from organs other than the breast, the types of cancer previously mentioned show similar molecular alterations than those found in mammary field cancerization Wistuba et al. (1999); Van Rees et al. (2000); Kadara and Wistuba (2012); Hawthorn et al. (2014); Patel et al. (2015). What the studies mentioned in the above paragraphs have in common is that they show evidence of variations in optical parameters, such as μ_s and γ, that were measured over extended areas of the organ, including regions away from tumor margins. Another important aspect in these studies is that they are not performed using X-rays. However, there is evidence that shows differences in the attenuation coefficients and trace elements composition between normal, malignant, and malignant adjacent tissue for this type of radiation Johns and Yaffe (1987); Soares et al. (2020); Silva et al. (2009), hence we consider it is not far fetched to hypothesize that the variation in optical properties of tissue affected by field cancerization can extend to the wavelengths used in mammography.

Consequently, if these changes in optical parameters are present over a sufficiently wide area, they may result in changes in the mammogram that could be detected via parenchymal analysis.

3. Materials and methods

To test the effects of our field cancerization model at the mammography image level, we required a tool for the generation of modifiable virtual breast phantoms and the simulation of digital mammography. We also analyzed these images to assess the impact of field cancerization. In this section we describe the tools used for the simulation phase, shown in figure 2, and the statistical tests used in the analysis phase, shown in figure 3.

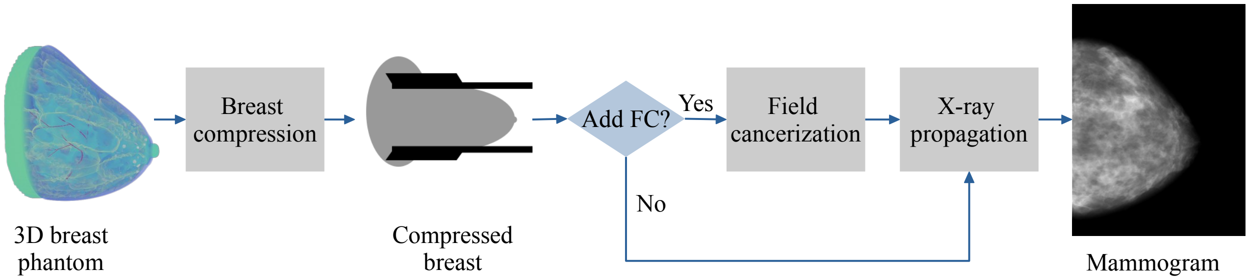

Figure 2. In the simulation step, we generate voxelized 3D virtual breast phantoms with and without field cancerization, and simulate craniocaudal mammography from each.

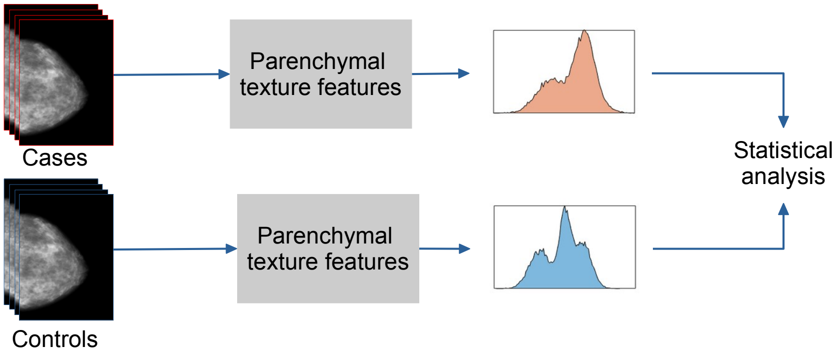

Figure 3. In the analysis step, we extract parenchymal texture features from the mammograms and test for their resemblance between cases and controls.

3.1. Mammography simulation

For the simulation of the phantoms and digital mammography, we used the simulation tool developed in the VICTRE project Badal et al. (2021); Badano et al. (2018). VICTRE was created to offer an in-silico alternative to expensive, time-consuming clinical trials; it has a complete, open-source pipeline that comprises several steps. The steps that pertain to mammography image simulation are: anthropomorphic breast phantom simulation, breast phantom compression, and X-ray imaging simulation. These steps are explained in the following subsections.

3.1.1. Anthropomorphic breast model. The VICTRE pipeline begins with the simulation of an anthropomorphic breast phantom Graff (2016). This voxelized phantom consists of skin, nipple, lactiferous ducts, terminal duct lobular units (TDLU), inter-lobular glandular tissue, fat, Cooper ligaments, chest muscles, and arteries and veins. Characteristics such as volume, fat percentage, skin thickness, maximum TDLU length, etc., are customizable, allowing the simulation of diverse breast morphologies. Additionally, random seeds are used to generate different phantoms with the same base characteristics, such as an equal amount of ducts and fat percentage. The voxel size used for the simulations was 0.05 mm.

3.1.2. Model of physical breast compression. Mammography acquisition requires the breast to be compressed between two paddles to reduce breast thickness and improve image quality. This step is performed in the VICTRE pipeline by the following steps:

1. A tetrahedral mesh is created in the volume of the phantom, using the open-source software TetGenSi (2015).

2. Elastic properties (Young's module and Poisson's ratio) are assigned to the *fatty* and *glandular* tissues. The tetrahedrons that contain pectoral muscles are set as fixed boundaries.

3. The tetrahedral version of the breast phantom and its properties are passed to the open-source software for computational biomechanics FeBiO Maas et al. (2012), which creates two compression paddles that come together, compressing the phantom to the desired thickness.

4. The compressed phantom is now a displaced map of the original tetrahedral node positions. This is then interpolated to locate the displaced voxels and return the phantom to its original voxelized form.

The software allows for selecting the desired compression thickness. However, this is constrained by the mechanical properties of the breast tissues.

3.1.3. X-ray imaging simulation. Mammography is a type of X-ray imaging specialized in detecting breast anomalies. Its functionality is based on the interaction of X-rays with the different mammary tissues. On a mammography examination, as mentioned above, the breast is compressed between two paddles. This helps image quality by preventing motion during the imaging; it evens out the thickness of the organ, which helps reduce the scattering interactions; and reduces the radiation dose the patient has to receive. All these conditions help improve diagnostic performance Poulos and McLean (2004); Robinson and Kotre (2008). The breast is then irradiated from one side with low-energy X-rays between 22 and 49 keV Diekmann et al. (2007). In digital mammography, the radiation that reaches the detector on the opposite side of the breast is converted into a usable signal, and the image is stored digitally.

As mentioned, mammography imaging captures the attenuated radiation that penetrates the breast. According to Fresnel theory, when radiation interacts with a dielectric medium with a refraction index greater than air, part of the radiation penetrates the medium, while a minor part is reflected. The radiation that penetrates the medium is either absorbed or scattered. Once the radiation is inside the medium, a way of studying its interaction with biological tissue consists on considering several points that are characterized by physical properties, such as absorption and scattering coefficients, that interact with the radiation Wang and Wu (2012). These attenuating processes are responsible for the energy loss when radiation goes through a medium and are the underlying phenomena that make it possible to characterize the different inner structures in a radiographic image. They are, however, also a source of image degradation.

The main means of interaction for x-ray penetrating biological tissue are Rayleigh scattering, Compton scattering, photoelectric absorption, and pair production. Their probability of occurrence depends on the x-ray energy range used:

- Rayleigh scattering occurs predominantly at low diagnostic energies. In mammography, it can account for more than 10% of attenuation Berggren et al. (2016). In this type of interaction, there is no ionization, ejected electrons, nor change in wavelength.

- Compton scattering is the predominant scattering interaction on medical x-ray imaging. This effect has a non-trivial contribution to image degradation since it reduces the perceived primary attenuation differences between the tissues; this is a loss in radiographic contrast. The incident photon energy is divided between the ejected electron and the scattered photon in this interaction.

- Photoelectric absorption is the scenario in which the incident photon is completely absorbed and an electron, named photoelectron, is ejected with the same energy as the incident photon, minus the binding energy. The ionized atom re-stabilization results in an energy release, either as characteristic x-rays or Auger electrons. Since there are no scattered photons, this type of interaction does not degrade the image.
- Pair production is usually of no consequence in mammography since it requires high energy radiation. In this case, the incident photon is converted into an electron-positron pair. The electron interacts and eventually becomes part of another atom, while the positron combines with an electron in an annihilation reaction that results in high-energy electromagnetic radiation.

We used the Monte Carlo x-ray transport simulation code MC-GPU Badal et al. (2021) for breast imaging simulation. This code was validated via measurement of the Modulation Transfer Function and comparing it to experimental results Badano et al. (2018); it was additionally tested using a digital quality control phantom and an ideal pinhole camera and comparing with experimental measurements Badal et al. (2021). Monte Carlo methods are computational algorithms used to estimate the outcome of a stochastic process. The transport of photons on tissue is a quantum phenomenon; hence the aforementioned processes, that are its working principles, are stochastic in nature. To simulate photon transport, a specific number of photons are simulated in the desired direction. The laws that govern the relevant interactions between these and the tissue are characterized by their probability distributions, and random sampling is used to decide the random path that each ray will follow.

The mentioned process is as follows: each photon initial state is characterized by a specific position $\mathbf{r} = (x,y,z)$, direction (given by the direction cosines) $\hat{\mathbf{d}} = (u,v,w)$ and energy E. On the event of an interaction, a new set of these values is calculated and adjudicated to the photon, so that for the n-th scattering event, the photon is in state $[\mathbf{r}_n, \hat{\mathbf{d}}_n, \mathrm{E}_n]$. The probability for the occurrence of the interactions mentioned above is determined by E; the random variables: type of interaction, length of the free flight, and scattering angle energy loss are randomly sampled from their corresponding probability distribution function (PDF) Salvat et al. (2006).

The PDFs used to sample the properties that characterize the interaction depend on the mean free path and nominal density of each tissue. To be able to simulate the photon propagation process on the more than ten different tissues and elements that can be simulated using VICTRE, the MC-GPU code uses the information contained in *material files*. These are files generated with the computer code system Penelope-2006 Salvat et al. (2006). They contain information on the mean free paths for Rayleigh, Compton, Photoelectric, and Pair production interactions for different photon energies and the nominal material densities.

Finally, MC-GPU uses the following simplifications inside the simulated breasts regarding the scattering events mentioned above, to increase the simulation speed: there are no secondary electron transport after photoelectric or Compton interactions, and there is no fluorescence emission inside the body.

Besides the photon transport, MC-GPU deals with the x-ray source and the detection grid.

The source is modeled as an extended source with a focal spot of 0.3mm, and the emission of x-rays is approximated by sampling from a gaussian distribution. The simulated detector includes a protective cover and anti-scatter grid, and binary random sampling is used to determine if the photons that reach the other side of the breast are absorbed or transmitted through the cover and grid.

3.2. Field cancerization model

As mentioned in section 2.2, the evidence shows that aberrations associated to field cancerization are present beyond the margins of cancer malignancy, and they are believed to even predate initial cancer signs. This evidence provides a starting point for the proposal of a model of field cancerization, suggesting that our model should not be constrained to the volume occupied by an average breast tumor, and that modifying the optical parameters of the tissues is a plausible route.

Additionally to the evidence already presented, some of the molecular aberrations of mammary field cancerization have been observed to follow a radial trend. This is to say, the “intensity” of the aberration observed in the histologically normal tissue diminishes with distance to the tumor Ellsworth et al. (2004b,a); Heaphy et al. (2006); Cheng AS, Culhane AC, Chan MW, Venkataramu CR, Ehrich M, Nasir A, Rodriguez BA, Liu J, Yan PS, Quackenbush J, Nephew KP, Yeatman TJ (2015). These studies have not been performed in a way that could hint a more specific geometric profile, and even under this circumstance, a direct translation between genetic aberration and a characteristic susceptible of implementation in our model is unknown. However, the fact that the alterations are not necessarily homogeneous but follow a radial trend, and them not being restricted to a reduced area are important characteristics that we also take into account.

We defined a model that conveyed the previous evidence, and would be implemented at the phantom level. To represent the evidence in the change of the optical parameters described in section 2.2 we introduced modifications in the form of scattering center, which would be distributed in the whole breast volume in a non-uniform way. Based on the evidence of the modifications intensity showing a radial tendency with respect to a cancerous lesion, we sampled the locations of our scattering center from a probability distribution, which we built in two steps according to the tissues considered:

First, for the majority of inner breast tissues, we defined a 3D normal distribution given by the probability density function:

$$\mathscr{B}(\vec{r};\vec{\mu},\Sigma) = b(\vec{r})\mathscr{N}(\vec{r};\vec{\mu},\Sigma)\,, \tag{1}$$

where:

$$\mathscr{N}(\vec{r};\vec{\mu},\Sigma) = \frac{1}{(2\pi)^{d/2}}|\Sigma|^{-1/2}\exp\left[-\frac{1}{2}(\vec{r}-\vec{\mu})\Sigma^{-1}(\vec{r}-\vec{\mu})^{T}\right], \tag{2}$$

$$b(\vec{r}) = \begin{cases} 0 \quad if \quad \vec{r} \quad \text{is outside of breast boundary or is duct,} \\ \\ 1 \quad if \quad \vec{r} \quad \text{is inside of breast boundary but not duct.} \end{cases} \tag{3}$$

in this equation, $\vec{r} \in \mathbb{R}^3$ is the variable and a spatial vector, $\vec{\mu} \in \mathbb{R}^3$ is a vector that locates the focal point of the distribution, and $\Sigma \in \mathbb{R}^{3\times 3}$ is the covariance matrix. We did not assume correlation between our spatial variables, so we used a diagonal matrix, hence the only non-zero elements are σ_x^2, σ_y^2 and σ_z^2, where σ stands for the standard deviation in each Cartesian direction. We assumed an isotropic distribution, which makes Σ a scalar matrix, with elements: σ^2.

Since our area of interest is risk assessment, we proposed a model for field cancerization at a stage that predates cancer signs, hence no cancerous lesions or micro calcifications were modeled. Instead, we picked a random location inside the breast as the mean $\vec{\mu}$ of our distribution of scattering center.

For the second part of our model, we took a special consideration for one breast component. Invasive ductal carcinoma is the most common type of breast cancer and it emerges from the cells of the mammary ducts, for this reason we decided to give a preferential treatment to this breast structure. We performed a similar operation to define the probability of the placement of the scattering centers in the ducts structure, selecting the same $\vec{\mu}$ as in the previous process:

$$\mathscr{D}\left(\vec{r};\vec{\mu},\Sigma_d\right) = d\left(\vec{r}\right)\mathscr{N}_d\left(\vec{r};\vec{\mu},\Sigma_d\right), \tag{4}$$

$$d\left(\vec{r}\right) = \begin{cases} 0 \quad if \quad \vec{r} \quad \text{is not duct,} \\ \\ 1 \quad if \quad \vec{r} \quad \text{is duct.} \end{cases} \tag{5}$$

The covariance matrix of this normal density is also a scalar matrix, with diagonal entries:

σ_d^2. A 2D illustration of the probability distributions for each part of our model can be seen in figure 4.

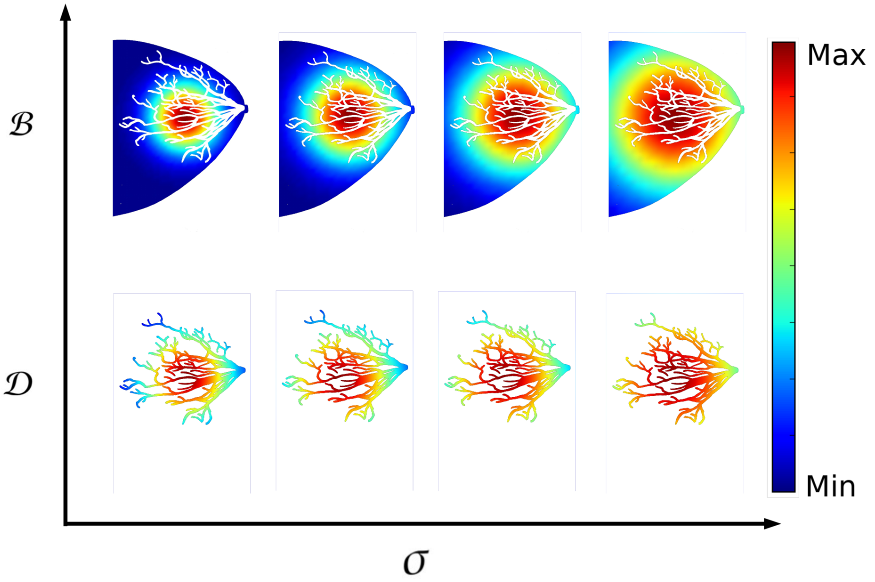

Figure 4. 2D representation of the probability functions from equations 1 and 4.

We implement the procedures involving equations 1 and 4 consecutively in each phantom, hence our full field cancerization model has the density function given by:

$$\mathscr{F}_{\mathscr{C}}(\vec{r};\vec{\mu},\Sigma,\Sigma_d) = \begin{cases} \mathscr{N}(\vec{r};\vec{\mu},\Sigma) & if \quad \vec{r} \quad \text{is inside of breast and not duct,} \\ \\ \mathscr{N}_d(\vec{r};\vec{\mu},\Sigma_d) & if \quad \vec{r} \quad \text{is duct,} \\ \\ 0 & \text{otherwise} \end{cases} \tag{6}$$

In summary, we transform a group of voxels into scattering center based on the density function 6.

We assigned the optical properties of a cancerous mass to characterize these scattering centers, this decision was based on the fact that the texture features of areas corresponding to tumor in mammography are denser and coarser than healthy tissue. Additionally, there is also evidence that, in the presence of field cancerization, areas of tumor and non-tumor show high percentage of textural similarity Baughan et al. (2021), so introducing the same type of scattering center in the breast phantom, albeit in a non-homogeneous way, will likely introduce coarseness in a broad area of the resulting image. With the point of illustrating the differences between the optical properties of the scattering centers and the different tissues where they were introduced, figure 5 shows the the mean free paths × nominal density for the different events.

3.3. Generation of our digital cohort

3.3.1. Control group. Using the simulation tool described in section 3.1, we generated a cohort of 60 digital voxelized breast phantoms. We will refer to this set of virtual breast phantoms as the *original cohort*, or controls. We simulated four different types of phantoms, according to the four glandularity types determined by the Breast Imaging-Reporting and Data System (BI-RADS) Atlas 5th edition D'Orsi (2014). This categorization not only takes into account the amount of relative fibroglandular tissue but also its apparent spatial distribution. To simulate a realistic glandularity distribution in a human cohort, we imitated the distribution of a cohort used in studies for screening mammography Pertuz et al. (2019a) to determine the number of breast phantoms of each category. These categories and the proportion of our cohort they comprise are

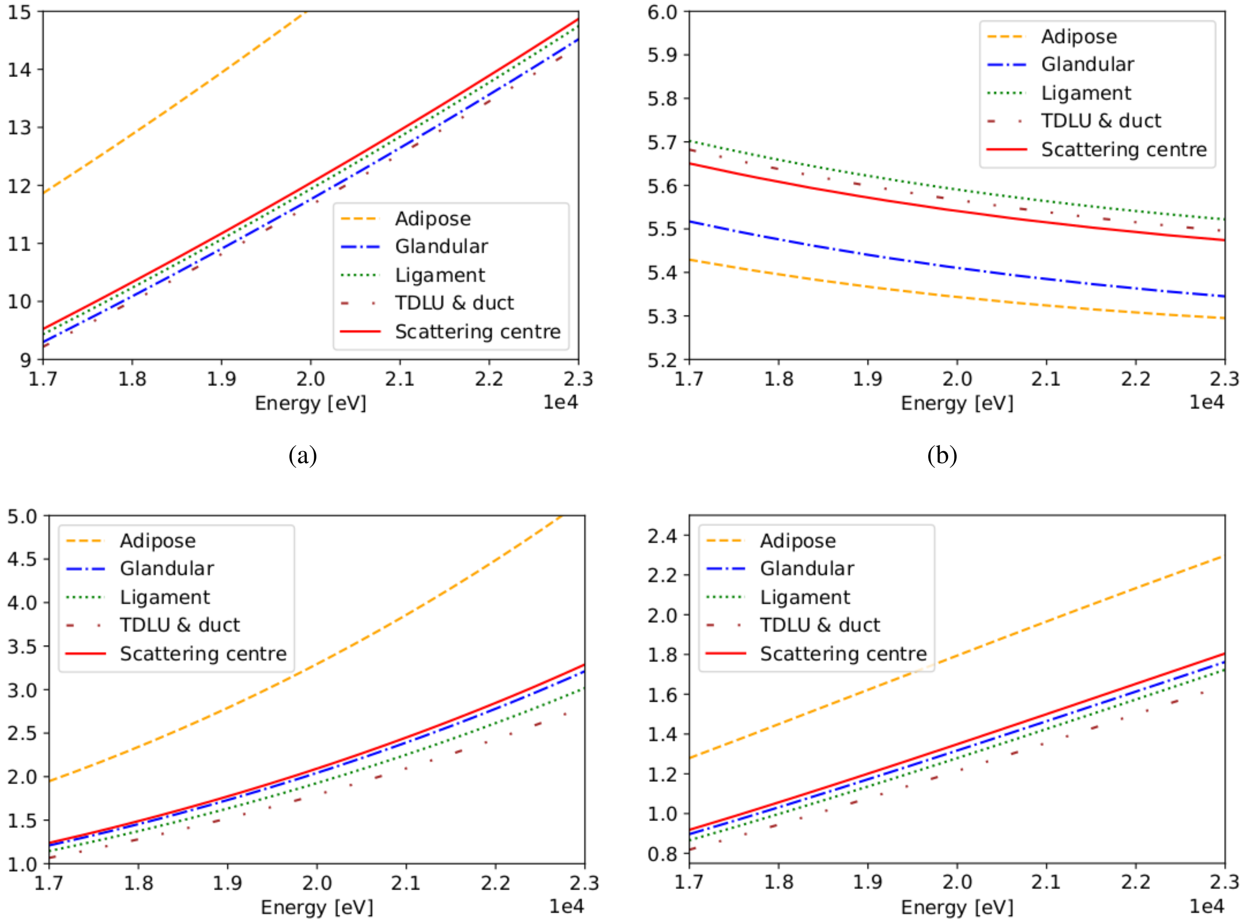

(a) (b)

(c) (d)

Figure 5. Mean free path × nominal density [g/cm^2] for the different breast tissues and the scattering centers (glandular) for the different interaction events: a) Rayleigh scattering, b) Compton scattering, c) Photoelectric absorption, and d) Pair production effect. TDLU: Terminal duct lobular units

dense (3%), heterogeneously dense (40%), scattered fibroglandularity (47%), and fatty (10%). An example of phantoms from each category are shown in figure 6.

We compressed and imaged this original cohort of breast phantoms as described in sections 3.1.2 and 3.1.3. The mammographic view simulated was craniocaudal. The original mammogram size is 3000×1500 pixels, and the pixel size is 85μm. The images were transformed from

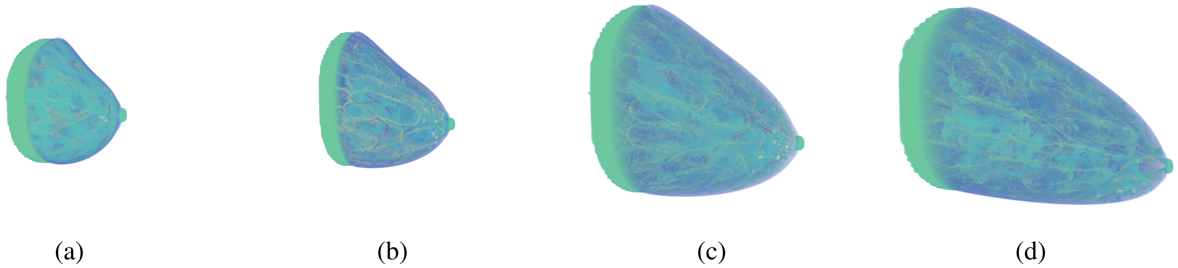

(a) (b) (c) (d)

Figure 6. Examples of the breast sizes simulated, in this case the size is related to the glandularity type. The images conserve their real aspect ratios between sizes. a) Dense breast. b) Heterogeneously dense breast. c) Breast with scattered fibroglandularity. d) Fatty breast.

raw to DICOM format and cropped to sizes 2010×1000 (for dense and heterogeneous type) and 2010×1500 (for scattered and fatty), this distinction was made due to the differences in the original images (see figure 7). Images were cropped to exclude the white border of each image, which interfered with the consequent step of ROI selection. This set of images conforms our *control* dataset.

3.3.2. Cases groups. We generated a series of *cases* by introducing our field cancerization model (section 3.2) on the compressed and cropped breast phantoms. We decided to implement the model in the already compressed and cropped phantom for two reasons: first, there is a significant amount of time required for the compression and cropping of the 60 phantoms (more than 70 hours), and second, any modifications that affect the fatty and glandular tissues of the non-compressed breast can lead to a different compressed breast thickness, which consequently affects the resulting images, and the features extracted from them. Since our analysis is based on these texture features, we strove to control any extra variable that could affect our simulated images, to better observe the effect of the field cancerization model by itself.

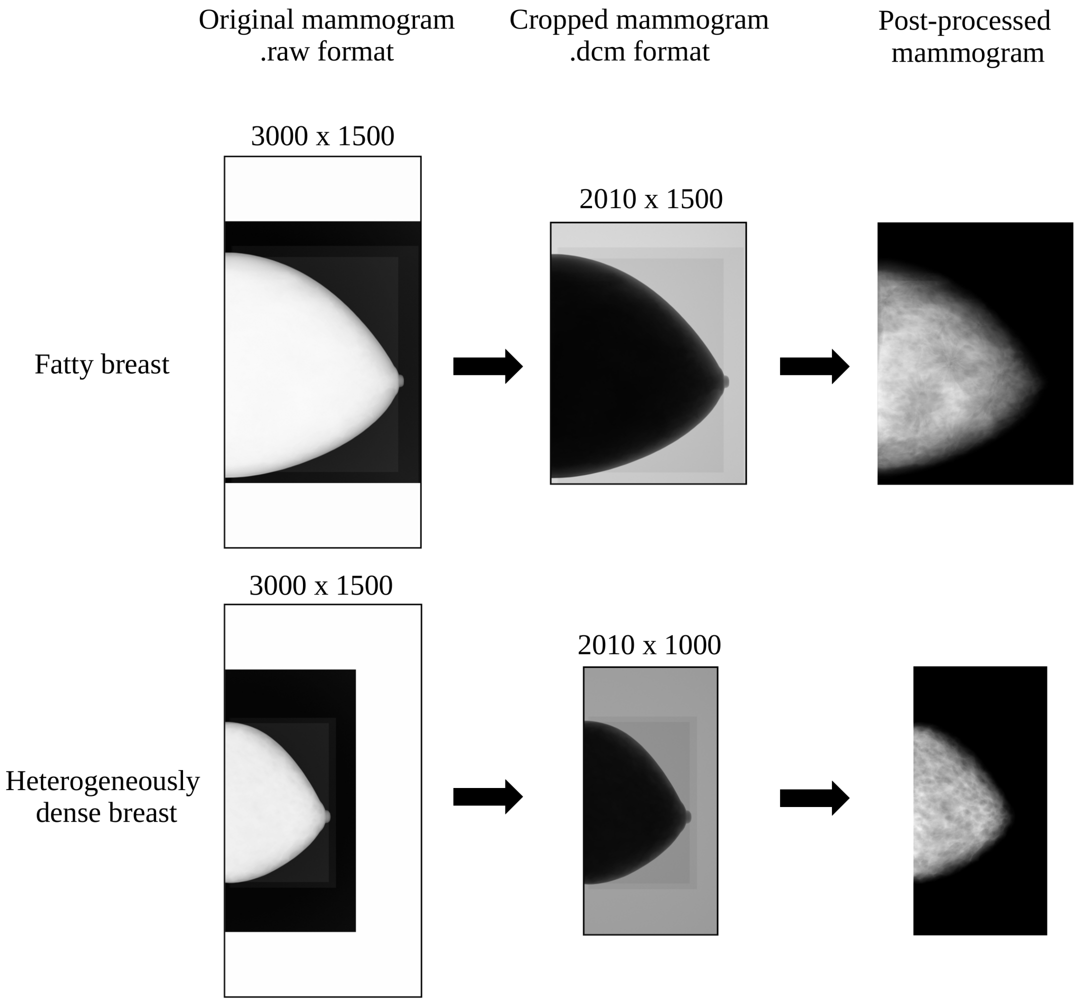

Figure 7. Conversion and cropping of the mammograms from raw to DICOM format. We use two different sizes due to the differences in the original image due to the breast size.

The phantoms generation and compression were executed on a machine with Intel® Xeon(R) W-2145 with 64GB RAM and the imaging through a GPU NVIDIA Quadro P2000, both in Ubuntu 20.04. Table 1 summarizes the simulation times for each phantom size and step. The cropping step, not mentioned above, consists on the cropping of the original volume to exclude as many air voxels as possible.

Table 1. Computation times for the different phantom sizes.

Process	Average time [h]			
	dense	heterogeneous	scattered	fatty
Phantom generation	0.8	1.5	3.0	4.4
Compression	0.4	0.6	1.2	1.8
Cropping	0.1	0.1	0.2	0.3
Imaging	0.5	0.7	1.1	2.5

3.4. Experiments

To determine the limit at which our field cancerization model is detectable, we performed exhaustive experiments with the following ranges of parameters: σ from 5 to 35 [mm], σ_d from 5 to 100 [mm] and average number of scattering centers from 27 to 632 [S/mm^3]. For discussion purposes, we have singled out the three *levels* showcased in table 2, which represent three scenarios of interest for our study: a level for which the field cancerization is not detectable (level I), a borderline scenario (level II), and a scenario where the effect is detectable (level III). We differentiate each level by their parameters, and assign them a letter for ease of reference.

Table 2. Parameters used for three specific modification levels.

Level	σ [mm]	σ_d [mm]	S/mm^3
I	35	50	47
II	35	50	317
III	35	100	632

After implementing each level of field cancerization, a number of voxels are transformed into scattering centers. The percentage that these comprise out of the whole phantom volume is presented in table 3, for the levels of modification singled out in table 2. Finally, table 5 shows an example per each breast type of the impact that these levels of modification have in the resulting mammogram.

Table 3. Mean percentage of the total breast area that ended up being modified at each level for each of the breast glandularity types simulated.

Level	Percentage modified [%]				average [%]
	dense	heterogeneous	scattered	fatty	
I	1.1	0.7	0.5	0.4	0.6
II	6.7	5.2	3.1	2.1	3.9
III	12.8	9.9	6.6	4.9	7.9

3.5. Statistical analysis

As mentioned in section 2.1, computerised models for breast cancer risk assessment take the parenchymal texture features extracted from the mammograms as input and produce an output: the assessment. This means that the information that yields the performance of these methods is encoded in the texture features of the image. Methods for computerised breast cancer risk assessment using mammography are usually classification algorithms; if the data used to train them, which is composed from cases and controls, has systemic characteristics or values that tell them apart, the algorithm must be able to classify an unseen subject.

To assess the extent of our field cancerization model's impact on the image texture features, and determine if the model introduces changes that would be statistically significant, we performed a series of tests between our control dataset and each of our cases. If our field cancerization model induces systemic differences in the images and these are identifiable via the analysis of these features, it would be sensible to think that elaborated classification models could use these differences for risk assessment.

Each of the following test is performed between the original 60 phantoms and the modified cases after the introduction of field cancerization. Following this, each test is performed with a datset of 120 images.

We selected a whole breast ROI (figure 1(a)) and extracted 33 parenchymal texture features (see table 4) from each image of our datasets, using the Software OpenBreast, which is a clinically validated software for processing digital mammography images Pertuz et al. (2019a).

3.5.1. Tests for statistical difference. We used three different tests that assess for statistically significant differences. First, for texture features that follow a normal distribution, a two-sample Student's t test was used King and Eckersley (2019a). The null hypothesis assumes that the variances and means of both samples are equal. For texture features that do not follow a normal distribution, a nonparametric Wilcoxon Signed Rank test is applied, under the null hypothesis that the distribution of the difference between the two samples comes from a distribution with zero median King and Eckersley (2019b). Lastly, for all texture features, we used a two-sample Kolmogorov-Smirnov (KS) test, which null hypothesis states that the texture feature in both samples comes from the same continuous distribution function. These tests are performed by comparing the p-value to the significance level selected.

3.5.2. Test for statistical equivalence. We used the KS test to assess for statistical equivalence in the following way. The KS test calculates the maximum difference between the cumulative distribution functions of the two samples. Being $F_1(x)$ and $F_2(x)$ the cumulative distribution functions of the feature x in the control and case group respectively, the KS statistic is given by:

$$KS = max(|F_1(x) - F_2(x)|). \tag{7}$$

Higher KS values indicate a greater difference between the two samples being compared. This value by itself can be compared to a critical value that is used as an equivalence margin Sheskin (2003). This way of using the KS statistic is designed to demonstrate equivalence between two groups, which makes its interpretation essentially different from the KS test itself and from other tests designed to demonstrate statistically significant differences Ahn et al. (2013).

3.5.3. Test for discriminability. A multinomial regression analysis with cross-validation was performed to discriminate cases and controls James et al. (2013). As described previously, parenchymal texture features are used to train supervised machine learning models for the task of breast cancer risk assessment. We used this simple classifier to observe the discriminability of our cohorts is a scenario similar to those of a real life trial. Lasso regularization was implemented to perform feature selection and avoid overfitting Tibshirani (1996).

4. Results

We performed KS test, t-test and Wilcoxon signed rank test, at a significance level of 0.05, using the parenchymal features presented in Table 4. From the p-value of the KS test in Table 4, only seven features (highlighted yellow and only at level III) had significant p-values, meaning we could reject the null hypothesis, and the differences between the distributions of these features are statistically significant between cases and controls. The p-value of the t-test and Wilcoxon test that were below the significance level are highlighted in orange in Table 4. As expected, the number of features for which the differences are statistically significant increases with increasing level of field cancerization.

Table 4. P-value of the KS test for each of he features evaluated and p-value of the similarity tests performed on the features. These are divided by feature groups: Type I: Statistical features, Type C: Co-occurence features, Type R: Run-length features, Type G: Spectral features.

	Feature		KS p-value			Similarity test		
	abbrv.	Name	Level			Level		
			I	II	III	I	II	III
Type I	imin	Minimum gray-level value	0.981	0.784	0.477	0.891	0.001	<0.001
	imax	Maximum gray-level value	0.981	0.629	0.784	0.304	0.849	0.560
	iavg	Mean gray-level value	1.000	0.345	0.039	<0.001	<0.001	<0.001
	iran	Gray-level range	0.981	0.784	0.477	0.449	0.034	0.006
	istd	Gray-level standard deviation	1.000	0.999	0.911	<0.001	<0.001	<0.001
	ient	Entropy	1.000	0.999	0.981	0.057	0.003	0.026
	iske	Skewness	1.000	0.629	0.039	<0.001	<0.001	<0.001
	ikur	Kurtosis	1.000	0.784	0.629	<0.001	<0.001	<0.001
	ip05	5-th percentile	1.000	0.477	0.039	<0.001	<0.001	<0.001
	ip30	30-th percentile	1.000	0.784	0.160	<0.001	<0.001	<0.001
	ip70	70-th percentile	0.999	0.345	0.022	0.759	0.237	0.042
	ip95	95-th percentile	1.000	0.784	0.345	0.832	0.455	0.133
	iba1	Balance 1	0.999	0.345	0.064	<0.001	<0.001	<0.001
	iba2	Balance 2	1.000	0.629	0.160	0.791	0.335	0.099
Type C	cene	Energy	1.000	0.999	0.999	0.948	0.894	0.869
	ccor	Correlation	0.999	0.999	0.981	0.885	0.914	0.783
	ccon	Contrast	1.000	0.784	0.345	0.331	<0.001	<0.001
	chom	Homogeneity	1.000	0.784	0.239	0.095	<0.001	<0.001
	cent	Entropy	0.999	0.999	0.981	0.914	0.885	0.715
Type R	rrln	Run-length non-uniformity	0.999	0.981	0.477	0.927	0.555	0.293
	rgln	Gray-level non-uniformity	1.000	0.911	0.981	0.873	0.680	0.544
	rlre	Long run emphasis	1.000	0.629	0.160	0.931	0.267	0.061
	rsre	Short run emphasis	1.000	0.784	0.160	0.985	0.295	0.078
	rrpe	Run percentage	1.000	0.784	0.160	0.948	0.285	0.066
	rhgr	High gray-level run	0.999	0.477	0.160	0.783	0.285	0.047
	rlgr	Low gray-level run	0.999	0.911	0.239	0.981	0.646	0.214
Type G	sgra	Squared gradient	0.999	0.629	0.345	<0.001	<0.001	<0.001
	stev	Gradient standard deviation	1.000	0.345	0.103	0.832	0.267	0.063
	slap	Modified laplacian	0.999	0.345	0.013	<0.001	<0.001	<0.001
	swas	Wavelet sum	1.000	0.345	0.013	<0.001	<0.001	<0.001
	swav	Wavelet variance	0.999	0.477	0.022	<0.001	<0.001	<0.001
	swar	Wavelet ratio	1.000	0.784	0.239	0.852	0.420	0.125
	fdim	Fractal dimension	1.000	0.784	0.345	0.860	0.548	0.335

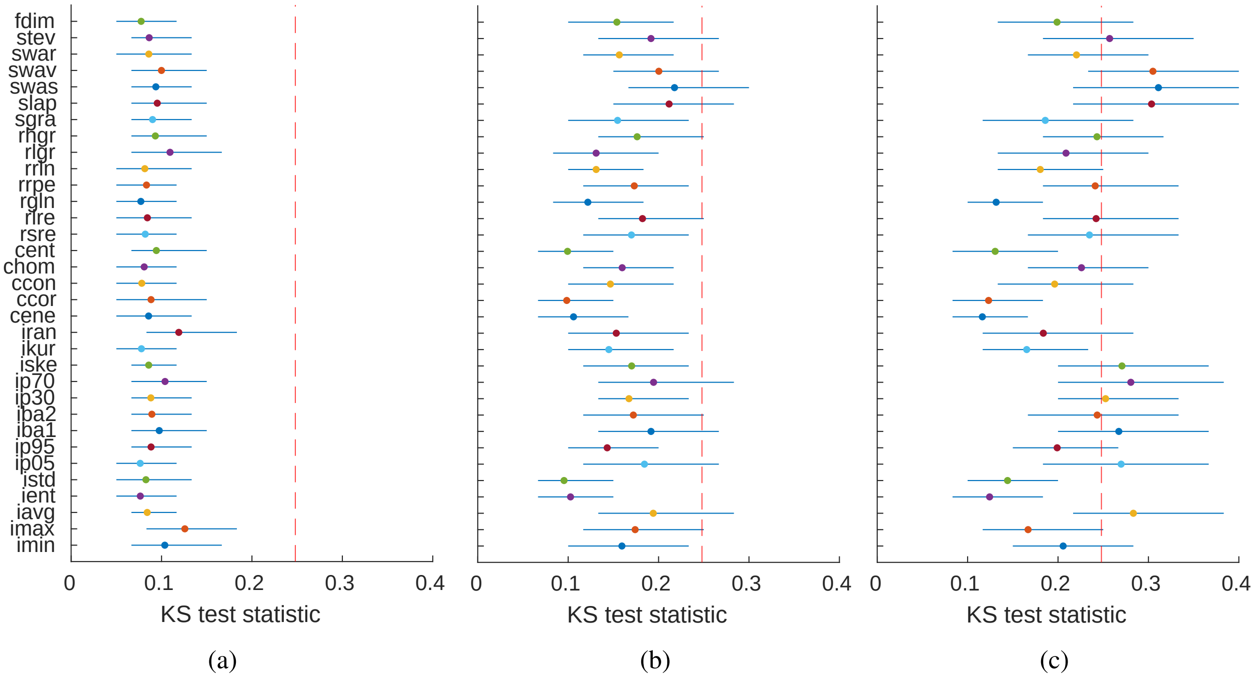

Figure 8. KS statistic and 95% CI, calculated with 2000 bootstrap iterations, for each feature at the three different field cancerization levels considered. The vertical red dotted line is the equivalent margin. a) Level I. b) Level II. c) Level III.

Comparison of the KS statistic to the similarity margin are shown in figure 8. In that figure, the statistic and 95% confidence intervals (CI) were calculated using 2000 bootstraps. For level I (Figure 8(a)), all features are equivalent between cases and controls. For level II (Figure 8(b)) all the point estimates of the KS statistic lay below the equivalence margin, however, some of the CI cross it. When part of the CI lies outside the equivalence margin, the control sample is not equivalent to the case sample, that is, there is no evidence of equivalence Ahn et al. (2013). For level III, most of the CI in Figure 8(c) cross the equivalence margin; of these, ten feature point estimates are above the equivalence margin, and includes all features that were statistically significant in the KS test, see Table 4.

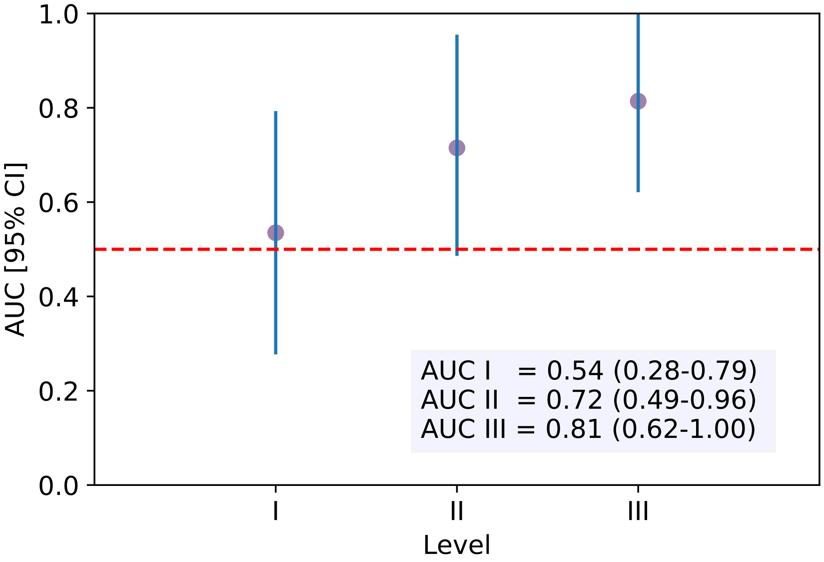

Figure 9. AUC and 95% confidence intervals for the classification model using the different levels of modification (X axis).

Regarding the regression analysis for the discrimination of field cancerization from parenchymal features, Figure 9 summarizes the classifier performance for the tree levels of field cancerization considered. The only model that had a statistically significant performance was level III. Performances using levels I and II were not statistically significant since the CI crosses the baseline value of 0.5. Additionally, we implemented Lasso regularization within the regressor, however only level III was fit for this process, where feature selection identified nine relevant features and obtained an AUC of 0.89 (0.75 - 1.00).

5. Discussion

In this study, field cancerization was modeled as non-local modifications spatially distributed around a foci. Following previous research findings about the behavior of field cancerization Bugter et al. (2019); Cheng AS, Culhane AC, Chan MW, Venkataramu CR, Ehrich M, Nasir A, Rodriguez BA, Liu J, Yan PS, Quackenbush J, Nephew KP, Yeatman TJ (2015); Damania et al. (2012); Ellsworth et al. (2004a,b); Heaphy et al. (2006); Spicer et al. (2016); Subramanian et al. (2009), its effect was modeled as a field of radially distributed alterations of the optical properties in the breast tissue. For the analysis of parenchymal features, we considered three scenarios with increasing level of field cancerization (see Table 3), which we refer to as level I, II and III.

We used the t-test, Wilcoxon test and KS test to assess for statistically significant differences between cases and controls, these results are summarized in Table 4. Level I, which introduces, in average, modifications that span less than 1% of the total breast volume, only showed some statistically significant results using the t-test (these are normally distributed features), meaning that while the mean and variance of the distributions of cases and controls might be statistically different, the same can not be said of the shape of their empirical cumulative distribution functions. Level II, with a mean percentage of modification just below 4% of the total breast volume, showed statistically significant differences using the t-test and Wilcoxon test. This can be interpreted in the same way as in level I. Finally, at level III, where the modifications occupy in average 7.9% of the breast volume, in addition to a high number of features showing statistically significant differences by the t-test and Wilcoxon test, 6 features (highlighted in yellow) showed statistically significant differences on their cumulative distribution functions, by the KS test.

We used the KS statistic and an equivalence margin to test for equivalence between cases and controls, these results are in figure 8. At level I, all of the features point estimates and CI lay below the equivalence margin, in which case similarity can not be denied. These low values of the KS statistic indicate that the differences between the cumulative distribution functions of the cases and control features were not greatly impacted by this level of field cancerization. At level II, 8 features CI cross the equivalence margin, this is, in principle, evidence to say that these features present non-equivalence. With field cancerization at level III, figure 8(c) showed that 30.3% of the features point estimate were above the equivalence margin. This is a high percentage of features that reject equivalence. This supports the affirmation that field cancerization at level III affects the image to such extent that several of the parenchymal texture features differ from the original in a statistically significant way.

We used multinomial regression analysis to test for the discriminability of the different levels of field cancerization considered (Figure 9). At level I, the modifications due to the field cancerization are not sufficient to allow for the discrimination of the images. At level II, the point estimate is above 0.5, but the CI lower limit still lays just under this baseline. This can be seen as a borderline case in which the consequences of field cancerization are reaching detectability. Finally, at level III, the differences are sufficient for the classification to have a high performance, which is also statistically significant. These results are consistent with our similarity and non-equivalence tests.

At this point, it is worth to remark that the alterations due to field cancerization at level III

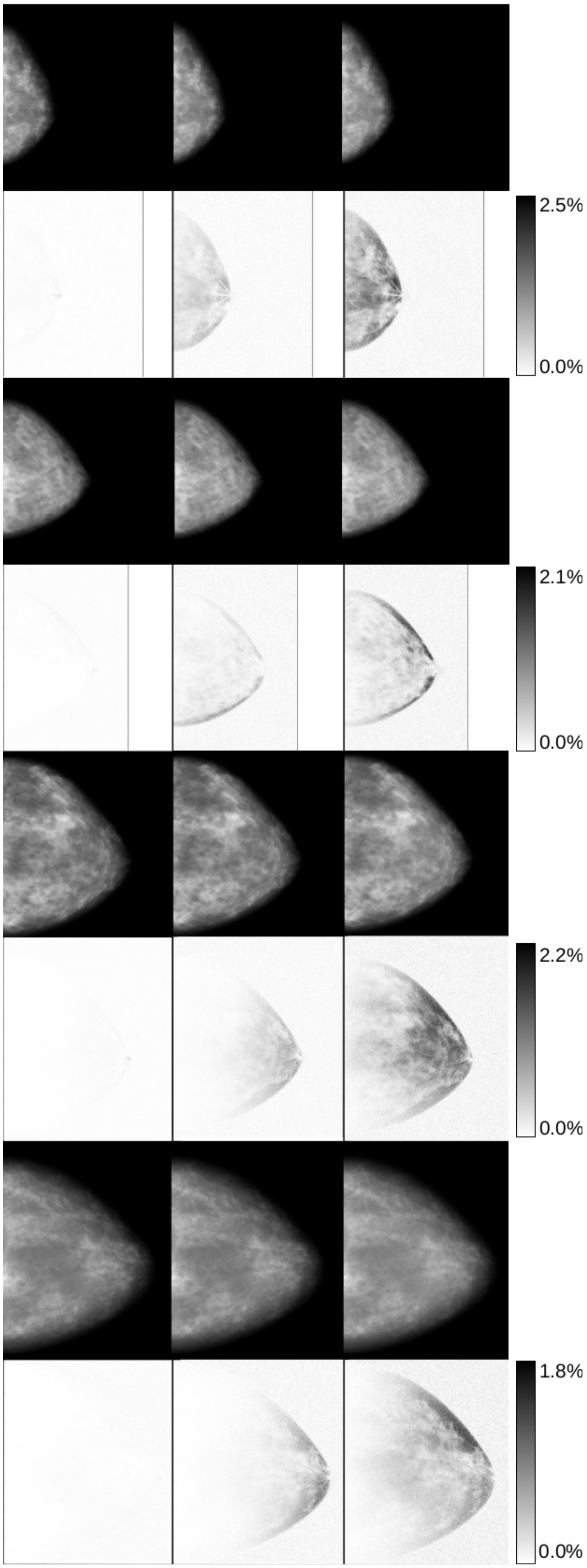

Table 5. Each couple of rows is an example of a type of phantom glandularity (from top to bottom: dense, heterogeneous, scattered and fatty). The top row of each pair is the mammogram with different levels of field cancerization for (from left to right: levels I, II, and III). The bottom row of each pair is the difference between the breast with field cancerization and the corresponding control. Differences are expressed as a percentage of the maximum gray level intensity of the original image. Intensities of difference images have been adjusted for visualization purposes.

are reached with modifications of percentages as low as 7.9% of the total volume of the breast phantom. This might seem like a negligible amount of modifications, however the scattering events, mainly of Compton nature, that result from this, suffice to have a greater impact in the resulting image. As illustrated in table 5, it is noticeable how the mammograms with field cancerization at the different levels are indistinguishable from the naked eye, however the differences are evident in the subtraction of the images. Level I results in very slight differences, while the impact of level II is clearly perceivable yet, as discussed above, not sufficient. Observing the case for level III, the comparison exhibits modifications that span the entire breast, suggesting, more than non-locality, a compromise of the entire breast before field cancerization could be detectable. Interestingly, the maximum difference in gray level reached for level III was of of around 2.2% of the original image maximum gray level value. This reiterates the idea that field cancerization in mammography is indistinguishable to the human eye, yet could be recognizable via computerized analysis. These results, especially at level III, support the hypothesis that field cancerization introduces changes in the radiological patterns of the mammograms, and these are evident via analysis of the parenchymal texture features of the image.

However, the limitations of our study need to be taken into account in the interpretation of these results. While the total volume of modifications were few in comparison to the total breast volume, the scattering centers used were impactful in some of the tissues, due to their inherent differences (see the differences between, for example, adipose tissue and scattering center tissue in figure 5). This could be a concern taking into account that it is likely that the changes in the optical parameters due to field cancerization are different in every type of tissue. In a real life scenario, the changes in the tissue parameters would be constrained by the nature of each of the tissue types, whereas the changes in the tissue would likely not be restricted to scattering centers. We consider that our model is a good first approximation in which we funneled large extensions of modifications in smaller volumes.

We need to address the concern of introducing scattering centers of very high volume, due to the randomness of the process of placing the scattering centers. Being a random process, the localization of the scattering centers made clusters in some cases, the largest of which comprised a volume of 11.7 [mm^3]. We assumed a pseudo spherical arrangement of these clusters and translated this volume to a projected area to compare with the smallest lesion size segmented in the mammography database INbreast Moreira et al. (2012). The area that our largest cluster comprised, 6.2 [mm^2], which was still smaller than the smallest lesion in the database, 14.5 [mm^2], giving us confidence that we did not simulate clusters large enough to mimic detectable lesions.

Equivalence tests for features whose CI crossed the equivalence margin but with point estimates below such margin warrant further discussion: These features are said to be non-equivalent, however a bigger sample size could reduce the length of the confidence interval, resulting in equivalence. This is the reason why we made the distinction between these features and those whose point estimate was above the equivalence margin when discussing level III.

Along these lines, one of the limitations of this study was the size of the cohort. Although the acquisition of synthetic data is usually faster than data from real patients, the simulation process was still time-consuming (refer to table 1 in section 3.3). A larger cohort might have resulted in more statistical power, which would benefit statistical analysis. This study was also bounded by the number of tissues allowed in the simulation software, limiting the field cancerization model to the introduction of one type of scattering center with fixed properties. Notice, however, that the generation of digital breast phantoms with these tissue types have been successfully used for virtual clinical trials Badano et al. (2018).

The geometry of the changes of optical parameters of the tissue resulting from the field cancerization effect is a tricky subject. Its characterization would require extensive testing of human breast tissue at numerous positions and the acquisition of these samples is not a trivial task, which explains why the experiments found in the literature were performed at only a couple of positions. If we wanted further evidence of the relationship of field cancerization and parenchymal analysis performance for the assessment of breast cancer risk, the testing would also need to be performed at the relevant wavelengths. Further research on the relation of the field cancerization effect and the evaluation of breast cancer risk through parenchymal analysis is imperative to understand the origins of the disease and the advantages it can have at the clinical level.

6. Conclusions

We proposed a model of the field cancerization effect by means of the introduction of scattering centers in an extensive volume of the breast. Using a virtual cohort of 60 normal breasts (controls) and 60 corresponding counterparts modified with field cancerization (cases), we tested several levels of field cancerization to find a configuration of parameters that would result in statistically significant differences in the textural patterns of the resulting images. Through the analysis of the parenchymal texture features of the image, we observed that, for an average amount of scattering centers corresponding to 7.9% of breast volume, the simulated mammograms obtained from these phantoms are not equivalent to those obtained from phantoms without field cancerization, and these two groups of images are discernible using multinomial analysis.

The extended but relatively small percentage of somewhat strong scattering centers were not perceivable by the human eye in the resulting mammograms, but performing a computerized analysis showed that they produced an impact enough to have statistical significance. These findings support our hypothesis of the feasibility of identifying breasts affected by field cancerization through parenchymal analysis.

Bibliography

Africano, G., Arponen, O., Sassi, A., Karivaara-Mäkelä, M., Holli-Helenius, K., Rinta-Kiikka, I., Lääperi, A.-L., and Pertuz, S. (2020). A comparison of regions of interest in parenchymal analysis for breast cancer risk assessment. In *2020 42nd Annual International Conference of the IEEE Engineering in Medicine & Biology Society (EMBC)*, pages 1136–1139. IEEE.

Ahn, C. K., Heo, C., Jin, H., and Kim, J. H. (2017). A novel deep learning-based approach to high accuracy breast density estimation in digital mammography. In *Medical Imaging 2017: Computer-Aided Diagnosis*, volume 10134, page 101342O. International Society for Optics and Photonics.

Ahn, S., Park, S. H., and Lee, K. H. (2013). How to demonstrate similarity by using noninferiority and equivalence statistical testing in radiology research. *Radiology*, 267(2):328–338.

Amadasun, M. and King, R. (1989). Textural features corresponding to textural properties. *IEEE Transactions on systems, man, and Cybernetics*, 19(5):1264–1274.

Amir, E., Evans, D., Shenton, A., Lalloo, F., Moran, A., Boggis, C., Wilson, M., and Howell, A. (2003). Evaluation of breast cancer risk assessment packages in the family history evaluation and screening programme. *Journal of medical genetics*, 40(11):807–814.

Antonelli, A., Meschino, G., and Ballarin, V. (2019). Mammographic density estimation through permutation entropy. In *World Congress on Medical Physics and Biomedical Engineering 2018*, pages 135–141. Springer.

Badal, A., Sharma, D., Graff, C. G., Zeng, R., and Badano, A. (2021). Mammography and breast tomosynthesis simulator for virtual clinical trials. *Computer Physics Communications*, 261:107779.

Badano, A., Graff, C. G., Badal, A., Sharma, D., Zeng, R., Samuelson, F. W., Glick, S. J., and Myers, K. J. (2018). Evaluation of digital breast tomosynthesis as replacement of full-field digital mammography using an in silico imaging trial. *JAMA network open*, 1(7):e185474–e185474.

Baughan, N. M., Li, H., Lan, L., Chan, C.-W., Embury, M., Whitman, G., El-Zein, R., Bedrosian, I., and Giger, M. L. (2021). Parenchymal field effect analysis for breast cancer risk assessment: evaluation of ffdm radiomic similarity. In *Medical Imaging 2021: Computer-Aided Diagnosis*, volume 11597, page 115970Z. International Society for Optics and Photonics.

Ben-Ari, R., Zlotnick, A., and Hashoul, S. (2016). A weakly labeled approach for breast tissue segmentation and breast density estimation in digital mammography. In *Proceedings - International Symposium on Biomedical Imaging*, volume 2016-June, pages 722–725. IEEE Computer Society.

Berggren, K., Danielsson, M., and Fredenberg, E. (2016). Rayleigh imaging in spectral mammography. *Medical Imaging 2016: Physics of Medical Imaging*, 9783:97830A.

Boyd, N. F., Guo, H., Martin, L. J., Sun, L., Stone, J., Fishell, E., Jong, R. A., Hislop, G., Chiarelli, A., Minkin, S., et al. (2007). Mammographic density and the risk and detection of breast cancer. *New England Journal of Medicine*, 356(3):227–236.

Boyd, N. F., Martin, L. J., Bronskill, M., Yaffe, M. J., Duric, N., and Minkin, S. (2010). Breast Tissue Composition and Susceptibility to Breast Cancer. *JNCI: Journal of the National Cancer Institute*, 102(16):1224–1237.

Bugter, O., van Brummelen, S., van der Leest, K., Aerts, J., Maat, A., de Jong, R. B., Amelink, A., and Robinson, D. (2019). Towards the optical detection of field cancerization in the buccal mucosa of patients with lung cancer. *Translational Oncology*, 12(12):1533–1538.

Byng, J. W., Yaffe, M. J., Lockwood, G. A., Little, L. E., Tritchler, D. L., and Boyd, N. F. (1997). Automated analysis of mammographic densities and breast carcinoma risk. *Cancer*, 80(1):66–74.

Campbell, R., Baker, E., Chippindale, A., Wilson, G., McLean, N., Soames, J., and Reed, M. (1995). Mri t staging of squamous cell carcinoma of the oral cavity: radiological-pathological correlation. *Clinical radiology*, 50(8):533–540.

Cheng AS, Culhane AC, Chan MW, Venkataramu CR, Ehrich M, Nasir A, Rodriguez BA, Liu J, Yan PS, Quackenbush J, Nephew KP, Yeatman TJ, H. T. (2015). Epithelial Progeny of Estrogen-Exposed Breast Progenitor Cells Display a Cancer-like Methylome. *Gerontology*, 61(6):515–525.

Chu, A., Sehgal, C. M., and Greenleaf, J. F. (1990). Use of gray value distribution of run lengths for texture analysis. *Pattern Recognition Letters*, 11(6):415–419.

Coleman, C. (2017). Early detection and screening for breast cancer. In *Seminars in oncology nursing*, volume 33, pages 141–155. Elsevier.

Curtius, K., Wright, N. A., and Graham, T. A. (2018). An evolutionary perspective on field cancerization. *Nature Reviews Cancer*, 18(1):19–32.

Damania, D., Roy, H. K., Subramanian, H., Weinberg, D. S., Rex, D. K., Goldberg, M. J., Muldoon, J., Cherkezyan, L., Zhu, Y., Bianchi, L. K., et al. (2012). Nanocytology of rectal colonocytes to assess risk of colon cancer based on field cancerization. *Cancer research*, 72(11):2720–2727.

Diekmann, F., Sommer, A., Lawaczeck, R., Diekmann, S., Pietsch, H., Speck, U., Hamm, B., and Bick, U. (2007). Contrast-to-noise ratios of different elements in digital mammography: evaluation of their potential as new contrast agents. *Investigative radiology*, 42(5):319–325.

D'Orsi, C. (2014). *2013 ACR BI-RADS Atlas: Breast Imaging Reporting and Data System*. American College of Radiology.

Dworkin, A. M., Huang, T. H.-M., and Toland, A. E. (2009). Epigenetic alterations in the breast: Implications for breast cancer detection, prognosis and treatment. In *Seminars in cancer biology*, volume 19, pages 165–171. Elsevier.

Ellsworth, D. L., Ellsworth, R. E., Liebman, M. N., Hooke, J. A., and Shriver, C. D. (2004a). Genomic instability in histologically normal breast tissues: Implications for carcinogenesis. *Lancet Oncology*, 5(12):753–758.

Ellsworth, D. L., Ellsworth, R. E., Love, B., Deyarmin, B., Lubert, S. M., Mittal, V., and Shriver, C. D. (2004b). Genomic patterns of allelic imbalance in disease free tissue adjacent to primary breast carcinomas. *Breast Cancer Research and Treatment*, 88(2):131–139.

Gabriel, J. (2007). What is cancer? In Gabriel, J. A., editor, *The Biology of Cancer*, chapter 1, pages 3–9. Wiley.

Gandomkar, Z., Suleiman, M. E., Demchig, D., Brennan, P. C., and McEntee, M. F. (2019). Bi-rads density categorization using deep neural networks. In *Medical Imaging 2019: Image Perception, Observer Performance, and Technology Assessment*, volume 10952, page 109520N. International Society for Optics and Photonics.

Gastounioti, A., Conant, E. F., and Kontos, D. (2016). Beyond breast density: a review on the advancing role of parenchymal texture analysis in breast cancer risk assessment. *Breast cancer research*, 18(1):1–12.

Gastounioti, A., Hsieh, M.-K., Cohen, E., Pantalone, L., Conant, E. F., and Kontos, D. (2018). Incorporating breast anatomy in computational phenotyping of mammographic parenchymal patterns for breast cancer risk estimation. *Scientific reports*, 8(1):1–10.

Graff, C. G. (2016). A new, open-source, multi-modality digital breast phantom. *Medical Imaging 2016: Physics of Medical Imaging*, 9783:978309.

Haralick, R. M., Shanmugam, K., and Dinstein, I. H. (1973). Textural features for image classification. *IEEE Transactions on systems, man, and cybernetics*, SMC-3(6):610–621.

Hartman, K., Highnam, R., Warren, R., and Jackson, V. (2008). Volumetric assessment of breast tissue composition from ffdm images. In *International Workshop on Digital Mammography*, pages 33–39. Springer.

Hawthorn, L., Lan, L., and Mojica, W. (2014). Evidence for field effect cancerization in colorectal cancer. *Genomics*, 103(2-3):211–221.

He, W., Harvey, S., Juette, A., Denton, E. R., and Zwiggelaar, R. (2016). Mammographic segmentation and density classification: A fractal inspired approach. In *Lecture Notes in Computer Science (including subseries Lecture Notes in Artificial Intelligence and Lecture Notes in Bioinformatics)*, volume 9699, pages 359–366. Springer Verlag.

He, W., Juette, A., Denton, E. R., Oliver, A., Martí, R., and Zwiggelaar, R. (2015). A review on automatic mammographic density and parenchymal segmentation. *International journal of breast cancer*, 2015.

Heaphy, C. M., Bisoffi, M., Fordyce, C. A., Haaland, C. M., Hines, W. C., Joste, N. E., and Griffith, J. K. (2006). Telomere DNA content and allelic imbalance demonstrate field cancerization in histologically normal tissue adjacent to breast tumors. *International Journal of Cancer*, 119(1):108–116.

Heaphy, C. M., Griffith, J. K., and Bisoffi, M. (2009). Mammary field cancerization: Molecular evidence and clinical importance. *Breast Cancer Research and Treatment*, 118(2):229–239.

Hernández, A., Miranda, D. A., and Pertuz, S. (2021). Algorithms and methods for computerized analysis of mammography images in breast cancer risk assessment. *Computer Methods and Programs in Biomedicine*, 212:106443.

Highnam, R., Brady, M., Yaffe, M. J., Karssemeijer, N., and Harvey, J. (2010). Robust breast composition measurement-volpara tm. In *International workshop on digital mammography*, pages 342–349. Springer.

Huo, Z., Giger, M. L., Wolverton, D. E., Zhong, W., Cumming, S., and Olopade, O. I. (2000). Computerized analysis of mammographic parenchymal patterns for breast cancer risk assessment: Feature selection. *Medical Physics*, 27(1):4–12.

James, G., Witten, D., Hastie, T., and Tibshirani, R. (2013). *An introduction to statistical learning*, chapter Classification. Springer.

Johns, P. C. and Yaffe, M. J. (1987). X-ray characterisation of normal and neoplastic breast tissues. *Physics in Medicine & Biology*, 32(6):675.

Kadara, H. and Wistuba, I. I. (2012). Field cancerization in non-small cell lung cancer implications in disease pathogenesis. *Proceedings of the American Thoracic Society*, 9(2):38–42.

King, A. P. and Eckersley, R. (2019a). *Statistics for biomedical engineers and scientists: How to visualize and analyze data*, chapter Inferential Statistics II: Parametric Hypothesis Testing. Academic Press.

King, A. P. and Eckersley, R. (2019b). *Statistics for biomedical engineers and scientists: How to visualize and analyze data*, chapter Inferential Statistics III: Nonparametric Hypothesis Testing. Academic Press.

Kontos, D., Winham, S. J., Oustimov, A., Pantalone, L., Hsieh, M.-K., Gastounioti, A., Whaley, D. H., Hruska, C. B., Kerlikowske, K., Brandt, K., et al. (2019). Radiomic phenotypes of mammographic parenchymal complexity: toward augmenting breast density in breast cancer risk assessment. *Radiology*, 290(1):41.

Lee, J. and Nishikawa, R. M. (2018). Automated mammographic breast density estimation using a fully convolutional network. *Medical physics*, 45(3):1178–1190.

Lehman, C. D., Yala, A., Schuster, T., Dontchos, B., Bahl, M., Swanson, K., and Barzilay, R. (2019). Mammographic breast density assessment using deep learning: clinical implementation. *Radiology*, 290(1):52–58.

Li, H., Giger, M. L., Huo, Z., Olopade, O. I., Lan, L., Weber, B. L., and Bonta, I. (2004). Computerized analysis of mammographic parenchymal patterns for assessing breast cancer risk: effect of roi size and location. *Medical physics*, 31(3):549–555.

Li, H., Giger, M. L., Huynh, B. Q., and Antropova, N. O. (2017). Deep learning in breast cancer risk assessment: evaluation of convolutional neural networks on a clinical dataset of full-field digital mammograms. *Journal of medical imaging*, 4(4):041304.

Li, H., Giger, M. L., Lan, L., Janardanan, J., and Sennett, C. (2014). Comparative analysis of image-based phenotypes of mammographic density and parenchymal patterns in distinguishing between {BRCA1/2} cases, unilateral cancer cases, and controls. *Journal of Medical Imaging*, 1(3).

Li, H., Giger, M. L., Olopade, O. I., and Lan, L. (2007). Fractal analysis of mammographic parenchymal patterns in breast cancer risk assessment. *Academic radiology*, 14(5):513–521.

Li, H., Mendel, K. R., Lan, L., Sheth, D., and Giger, M. L. (2019a). Digital mammography in breast cancer: additive value of radiomics of breast parenchyma. *Radiology*, 291(1):15.

Li, H., Mukundan, R., and Boyd, S. (2019b). Breast density classification using multifractal spectrum with histogram analysis. In *2019 International Conference on Image and Vision Computing New Zealand (IVCNZ)*, pages 1–6. IEEE.

Liu, Y., Azizpour, H., Strand, F., and Smith, K. (2020). Decoupling inherent risk and early cancer signs in image-based breast cancer risk models. In *International Conference on Medical Image Computing and Computer-Assisted Intervention*, pages 230–240. Springer.

Maas, S. A., Ellis, B. J., Ateshian, G. A., and Weiss, J. A. (2012). FEBio: Finite elements for biomechanics. *Journal of Biomechanical Engineering*, 134(1).

McCormack, V. A. and dos Santos Silva, I. (2006). Breast Density and Parenchymal Patterns as Markers of Breast Cancer Risk: a Meta-analysis. *Cancer Epidemiology Biomarkers & Prevention*, 15(6):1159–1169.

Miranda, D. A. and Pertuz, S. (2020). Field cancerization in the understanding of parenchymal analysis of mammograms for breast cancer risk assessment. *Medical Hypotheses*, 136:109511.

Moreira, I. C., Amaral, I., Domingues, I., Cardoso, A., Cardoso, M. J., and Cardoso, J. S. (2012). Inbreast: toward a full-field digital mammographic database. *Academic radiology*, 19(2):236–248.

Nebbia, G., Mohamed, A., Chai, R., Zheng, B., Zuley, M., and Wu, S. (2019). Deep learning of sub-regional breast parenchyma in mammograms for localized breast cancer risk prediction. In *Medical Imaging 2019: Computer-Aided Diagnosis*, volume 10950, page 109502P. International Society for Optics and Photonics.

Nonn, L., Ananthanarayanan, V., and Gann, P. H. (2009). Evidence for field cancerization of the prostate. *The Prostate*, 69(13):1470–1479.

Patel, A., Tripathi, G., Gopalakrishnan, K., Williams, N., and Arasaradnam, R. P. (2015). Field cancerisation in colorectal cancer: A new frontier or pastures past? *World Journal of Gastroenterology*, 21(13):3763–3772.

Pertuz, S., Sassi, A., Holli-Helenius, K., Kämäräinen, J., Rinta-Kiikka, I., Lääperi, A.-L., and Arponen, O. (2019a). Clinical evaluation of a fully-automated parenchymal analysis software for breast cancer risk assessment: A pilot study in a finnish sample. *European journal of radiology*, 121:108710.

Pertuz, S., Torres, G. F., Tamimi, R. M., and Kamarainen, J. (2019b). Open Framework for Mammography-based Breast Cancer Risk Assessment. In *IEEE International Conference on Biomedical and Health Informatics*, page pp, Chicago, USA. Institute of Electrical and Electronics Engineers (IEEE).

Poulos, A. and McLean, D. (2004). The application of breast compression in mammography: a new perspective. *Radiography*, 10(2):131–137.

Rivenbark, A. G. and Coleman, W. B. (2012). Field cancerization in mammary carcinogenesis - Implications for prevention and treatment of breast cancer. *Experimental and Molecular Pathology*, 93(3):391–398.

Robinson, M. and Kotre, C. (2008). Trends in compressed breast thickness and radiation dose in breast screening mammography. *The British Journal of Radiology*, 81(963):214–218.

Salvat, F., Fernández-Varea, J. M., and Sempau, J. (2006). Penelope-2006: A code system for monte carlo simulation of electron and photon transport. In *Workshop proceedings*, volume 4, pages 35–50. Nuclear Energy Agency, Organization for Economic Co-operation and . . . .

Shen, L., Kondo, Y., Rosner, G. L., Xiao, L., Hernandez, N. S., Vilaythong, J., Houlihan, P. S., Krouse, R. S., Prasad, A. R., Einspahr, J. G., Buckmeier, J., Alberts, D. S., Hamilton, S. R., and Issa, J.-P. J. (2005). MGMT Promoter Methylation and Field Defect in Sporadic Colorectal Cancer. *JNCI: Journal of the National Cancer Institute*, 97(18):1330–1338.

Sheskin, D. J. (2003). *Handbook of parametric and nonparametric statistical procedures*, chapter Inferential statistical tests employed with two independent samples. Chapman and Hall/CRC.

Si, H. (2015). TetGen, a delaunay-based quality tetrahedral mesh generator. *ACM Transactions on Mathematical Software*, 41(2).

Siegel, R. L., Miller, K. D., Fuchs, H. E., and Jemal, A. (2022). Cancer statistics, 2022. *CA: a cancer journal for clinicians*.

Silva, M., Tomal, A., Perez, C., Ribeiro-Silva, A., and Poletti, M. (2009). Determination of ca, fe, cu and zn and their correlations in breast cancer and normal adjacent tissues. *X-Ray Spectrometry: An International Journal*, 38(2):103–111.

Slaughter, D. P., Southwick, H. W., and Smejkal, W. (1953). “field cancerization” in oral stratified squamous epithelium. clinical implications of multicentric origin. *Cancer*, 6(5):963–968.

Soares, L. D. H., Gobo, M. S. d. S., and Poletti, M. E. (2020). Measurement of the linear attenuation coefficient of breast tissues using polienergetic x-ray for energies from 12 to 50 kev and a silicon dispersive detector. *Radiation Physics and Chemistry*, 167:108226.

Spicer, G. L., Azarin, S. M., Yi, J., Young, S. T., Ellis, R., Bauer, G. M., Shea, L. D., and Backman, V. (2016). Detection of extracellular matrix modification in cancer models with inverse spectroscopic optical coherence tomography. *Physics in Medicine & Biology*, 61(19):6892.

Subramanian, H., Pradhan, P., Liu, Y., Capoglu, I. R., Rogers, J. D., Roy, H. K., Brand, R. E., and Backman, V. (2009). Partial-wave microscopic spectroscopy detects subwavelength refractive index fluctuations: an application to cancer diagnosis. *Optics letters*, 34(4):518–520.

Tibshirani, R. (1996). Regression shrinkage and selection via the lasso. *Journal of the Royal Statistical Society: Series B (Methodological)*, 58(1):267–288.

Tzikopoulos, S. D., Mavroforakis, M. E., Georgiou, H. V., Dimitropoulos, N., and Theodoridis, S. (2011). A fully automated scheme for mammographic segmentation and classification based on breast density and asymmetry. *computer methods and programs in biomedicine*, 102(1):47–63.

Ushijima, T. (2007). Epigenetic field for cancerization. *BMB Reports*, 40(2):142–150.

van Engeland, S., Snoeren, P., Huisman, H., Boetes, C., and Karssemeijer, N. (2006). Volumetric breast density estimation from full-field digital mammograms. *IEEE Transactions on Medical Imaging*, 25(3):273–282.

Van Rees, B. P., Cleton-Jansen, A. M., Cense, H. A., Polak, M. M., Clement, M. J., Drillenburg, P., Van Lanschot, J. J., and Offerhaus, G. J. A. (2000). Molecular evidence of field cancerization in a patient with 7 tumors of the aerodigestive tract. *Human Pathology*, 31(2):269–271.

Wang, L. V. and Wu, H.-i. (2012). *Rayleigh Theory and Mie Theory for a Single Scatterer*, chapter 2, pages 17–21. John Wiley & Sons.

Wang, X., Huang, Y., Li, L., Dai, H., Song, F., and Chen, K. (2018). Assessment of performance of the gail model for predicting breast cancer risk: a systematic review and meta-analysis with trial sequential analysis. *Breast Cancer Research*, 20(1):1–19.

Wistuba, I. I., Behrens, C., Milchgrub, S., Bryant, D., Hung, J., Minna, J. D., and Gazdar, A. F. (1999). Sequential molecular abnormalities are involved in the multistage development of squamous cell lung carcinoma. *Oncogene*, 18(3):643–650.

Wolfe, J. N. (1976). Breast parenchymal patterns and their changes with age. *Radiology*, 121(3):545–552.

Yan, P. S., Venkataramu, C., Ibrahim, A., Liu, J. C., Shen, R. Z., Diaz, N. M., Centeno, B., Weber, F., Leu, Y.-W., Shapiro, C. L., et al. (2006). Mapping geographic zones of cancer risk with epigenetic biomarkers in normal breast tissue. *Clinical cancer research*, 12(22):6626–6636.

Zheng, Y., Keller, B. M., Ray, S., Wang, Y., Conant, E. F., and Kontos, D. (2015). Parenchymal texture analysis in digital mammography: a fully automated pipeline for breast cancer risk assessment. *Medical Physics*, 42(7):4149–4159.